Enhanced Nanogel Formulation Combining the Natural Photosensitizer Curcumin and *Pectis brevipedunculata* (Asteraceae) Essential Oil for Synergistic Leishmaniasis Therapy

Lara Maria Oliveira Campos , Estela Mesquita Marques , Daniele Stéfanie Sara Lopes Lera-Nonose , Maria Julia Schiavon Gonçalves , Maria Valdrinez Campana Lonardoni , Glécilla Colombelli de Souza Nunes , Gustavo Braga , And Renato Sonchini Gonçalves [*]

Article

Enhanced Nanogel Formulation Combining the Natural Photosensitizer Curcumin and *Pectis brevipedunculata* (Asteraceae) Essential Oil for Synergistic Leishmaniasis Therapy

Lara Maria Oliveira Campos [1], Estela Mesquita Marques [1], Daniele Stéfanie Sara Lopes Lera-Nonose [2], Maria Julia Schiavon Gonçalves [2], Maria Valdrinez Campana Lonardoni [2], Gléécilla Colombelli de Souza Nunes [3], Gustavo Braga [4] and Renato Sonchini Gonçalves [1,*]

1. Laboratory of Chemistry of Natural Products, Department of Chemistry, Federal University of Maranhão (UFMA), São Luís 65080-805, Brazil;
2. Department of Clinical Analysis and Biomedicine, State University of Maringá (UEM), Maringá 87020-900, Brazil;
3. Research Nucleus in Pharmaceutical Sciences Program, State University of Maringá (UEM), Maringá 87020-900, Brazil;
4. Federal University of Maranhão (UFMA), University College (COLUN), São Luís 65080-805, Brazil.
* Correspondence: renato.sg@ufma.br; Tel.: +55-98-9851-49235

Abstract: Neglected tropical diseases (NTDs), such as leishmaniasis, remain a global health challenge due to limited therapeutic options and rising drug resistance. In this study, we developed an advanced nanogel formulation incorporating curcumin (CUR) and *Pectis brevipedunculata* essential oil (OE*Pb*) within an F127/Carbopol 974P matrix to enhance bioavailability and therapeutic efficacy against *Leishmania (Leishmania) amazonensis* (*LLa*) promastigotes. The chemical composition of OE*Pb* was characterized using GC-MS and NMR, confirming the presence of major bioactive monoterpenes, including neral, geranial, α-pinene, and limonene. The nanogel formulation (nG*P*C) was optimized to ensure thermosensitivity, and stability, exhibiting a sol-gel transition at physiological temperatures. Rheological analysis revealed that nG*P*C exhibited Newtonian behavior at 5 °C, transitioning to shear-thinning and thixotropic characteristics at 25 and 32 °C, respectively. This behavior facilitates application and controlled drug release, making it ideal for topical formulations. Dynamic light scattering (DLS) analysis demonstrated that nG*P*C maintained a stable nanoscale structure with hydrodynamic diameters below 300 nm, while Fourier-transform infrared spectroscopy (FTIR) confirmed strong molecular interactions between OE*Pb*, CUR, and the polymer matrix. Biological assays demonstrated that nG*P*C significantly enhanced anti-promastigote activity compared to free CUR and OE*Pb*. At the highest tested concentration (17.5 μg/mL OE*Pb* and 50 μg/mL CUR, nGPC induced over 88% mortality in *LLa* promastigotes across 24, 48, and 72 h, indicating sustained efficacy. Even at lower concentrations, nG*P*C retained dose-dependent activity, suggesting a synergistic effect between CUR and OE*Pb*. These findings highlight the potential of nG*P*C as an innovative nanocarrier for leishmaniasis treatment. Future studies will investigate the underlying mechanisms of this synergism and explore the potential application of photodynamic therapy (PDT) to further enhance therapeutic outcomes.

Keywords: Leishmaniasis; *Pectis brevipedunculata* essential oil; curcumin

1. Introduction

Neglected tropical diseases (NTDs) represent a critical global health challenge, disproportionately affecting populations in tropical and subtropical regions, often living under conditions of extreme poverty [1]. Over one billion individuals are estimated to be impacted by NTDs, including conditions such as leishmaniasis, Chagas disease, and lymphatic filariasis [2]. These diseases are associated with significant morbidity, prolonged disability, and substantial economic costs. Despite their widespread prevalence and the immense burden they impose, NTDs remain largely neglected in the global health

agenda, facing barriers such as limited funding, insufficient drug development, the rise of drug resistance, and challenges in vector control [3–5]. These complexities underscore the urgent need for novel therapeutic strategies to address conventional treatments' limitations, particularly through innovative delivery systems that provide targeted, accessible, and effective solutions [6,7].

Leishmania (Leishmania) amazonensis (*LLa*) is one of the most prevalent protozoan parasites responsible for cutaneous leishmaniasis in the Americas, including Brazil, Peru, and other Latin American countries [8,9]. Transmitted by the bite of infected Lutzomyia, *LLa* primarily affects the skin, causing the formation of painful lesions or ulcers. If left untreated, these lesions can progress into chronic wounds, leading to irreversible scarring and, in some cases, mucocutaneous leishmaniasis [10]. The parasite's ability to invade and replicate within macrophages, which are essential for immune defense, complicates the host's immune response, allowing the infection to persist. While conventional therapies like pentavalent antimonials and miltefosine are available, their effectiveness is often limited by increasing drug resistance, side effects, and the need for prolonged treatment [11]. As a result, there is a pressing demand for alternative therapeutic strategies, particularly those leveraging advanced drug delivery systems such as nanogels, which can enhance drug efficacy and target the parasite more specifically [12–14].

Natural products, particularly essential oils (EOs) from plants native to the Amazon rainforest, have gained significant attention as promising therapeutic agents for NTDs. These oils, rich in bioactive molecules such as terpenoids and phenolic compounds, exhibit potent antimicrobial, antiparasitic, and anti-inflammatory properties, making them ideal candidates for addressing diseases like leishmaniasis [15,16]. The combination of EOs from different plant species or the incorporation of plant extracts into EO formulations has been shown to create synergistic or complementary effects, amplifying their therapeutic potential while minimizing the adverse side effects associated with conventional drugs. By utilizing the complex array of bioactive compounds in these natural products, researchers can develop more robust, effective, and targeted treatments for NTDs [17–22].

In this context, we hypothesize that a nanogel formulation based on the F127 copolymer and Carbopol 974P, loaded with low concentrations of *Pectis brevipedunculata* EO (EO*Pb*) and curcumin (CUR), will exhibit synergistic effects *in vitro* against *LLa* promastigote cells. *Pectis brevipedunculata* (Asteraceae), a plant native to the tropical and subtropical regions of the Americas, is known for its anti-inflammatory, antimicrobial, and antiparasitic properties [14,23]. Its EO, rich in monoterpenes like neral, geranial, α-pinene, and limonene, has shown potent antimicrobial activity, positioning the plant as a valuable source of natural agents for treating parasitic infections [24,25]. Previous studies from our group have demonstrated that EO*Pb*-loaded nanogels possess effective larvicidal, leishmanicidal, and anti-inflammatory activities, without cytotoxic effects [13,14]. In parallel, CUR, derived from *Curcuma longa*, is a well-established compound with proven leishmanicidal effects and has been extensively studied for its ability to inhibit parasite growth, modulate immune responses, and reduce inflammation. CUR's low toxicity and antioxidant properties further enhance its potential as a therapeutic agent [26–30].

This study aimed to evaluate the therapeutic potential of CUR and OE*Pb* incorporated into an F127/974P nanogel matrix at low concentrations, assessing their effectiveness against *LLa* promastigotes. The cytotoxicity of these compounds was specifically evaluated at concentrations below 2 mg of OE*Pb* and 0.7 mg of CUR, both for nanogels containing isolated bioactive compounds and for their combinations. The results revealed that while the free compounds (CUR- or OE*Pb*-loaded nanogel) showed limited activity, the nanogel formulation containing both (CUR/OE*Pb*-loaded nanogel) demonstrated significant anti-promastigote effects, with dose-dependent mortality of *LLa* promastigote cells. These findings indicate a potential synergistic interaction between the two compounds, which, upon encapsulation in the nanogel, contributed to an enhanced therapeutic efficacy. Future investigations will focus on elucidating the mechanisms driving this synergism and exploring the potential of PDT to further optimize treatment strategies for leishmaniasis.

2. Materials and Methods

2.1. Materials

Pluronic F127 (poly(ethylene oxide)-poly(propylene oxide)-poly(ethylene oxide)) triblock copolymer (MW = 12600 g/mol; $EO_{99}PO_{67}EO_{99}$), ultrapure water, anhydrous sodium sulfate (≥99%), sodium chloride, curcumin (≥99%), XTT (2,3-bis(2-methoxy-4-nitro-5-sulfophenyl)-5-[(phenylamino)carbonyl]-2H-tetrazolium hydroxide)), PMS (N-methyl dibenzopyrazine methyl sulfate), penicillin, streptomycin, fetal bovine serum and amphotericin B were commercially acquired from the Merck company (Rahway, NJ, USA). Carbopol 974P NF polymer was provided by IMCD114 Brasil (São Paulo, SP, Brazil)

2.2. Plant Material

The herbaceous plant *Pb* was gathered from the campus of the Universidade Federal do Maranhão (UFMA) in São Luís, Maranhão, Brazil, located at coordinates 2°33'20.5"S and 44°18'32.7"W. A voucher specimen (No. 5287) was submitted to the Rosa Mochel Herbarium (SLUI) at the Universidade Estadual do Maranhão (UEMA) in São Luís, MA, Brazil. The plant collection was conducted by Brazilian biodiversity protection regulations, registered under SisGen code AAFB38B.

2.3. Extraction Procedure

The extraction of EO*Pb* was performed via hydrodistillation using a Clevenger-type apparatus [13]. A total of 300 g of air-dried plant material was finely chopped with pruning shears to enhance extraction efficiency. The fragmented material was placed in a flask containing 500 mL of distilled water, and the hydrodistillation process was conducted for 2.5 hours following the onset of reflux. After extraction, the resulting oil/water (O/W) mixture was centrifuged at 3500 rpm for 10 minutes at 25 °C. To eliminate residual moisture, the oil phase was treated with anhydrous sodium sulfate. The final yield of EO*Pb*, calculated based on the initial dry weight of the plant material, was 0.81%.

2.4. CG-MS Analyses of EOPb

The characterization of OE*Pb* was performed using GC–MS and NMR techniques, adhering to established protocols [13]. In summary, GC and GC-MS analyses were carried out on Shimadzu systems, employing an RXi-1MS fused capillary column with helium as the carrier gas. The temperature gradient was optimized, and the samples (10 mg/mL in CH_2Cl_2) were injected at a 1:50 split ratio. Retention indices were determined using a homologous series of n-alkanes, and peak areas and retention times were recorded to estimate the relative proportions of components. GC–MS analyses were conducted using a Shimadzu QP2010 SE system with an AOC-20i auto-injector under the same conditions applied in GC. The EO constituents were identified by comparing their retention times, retention indices, and mass spectra with spectral libraries (ADAMS and FFNSC) and literature references. NMR spectra (^1H, ^{13}C, and DEPT-^{13}C) were obtained on a BRUKER Avance III HD spectrometer (11.75 Tesla, operating at 500.13 MHz for ^1H and 125.76 MHz for ^{13}C). Samples were prepared in deuterated chloroform ($CDCl_3$), with chemical shifts expressed in ppm relative to tetramethylsilane (TMS) as the internal standard.

2.5. Preparation of Nanogels

The nanostructured formulations were prepared according to the methodology described by Schmolka, using a cold procedure [13,14]. A portion of the F127 copolymer was slowly incorporated into distilled water, which was kept in an ice bath at 5-10 ºC. The solution was maintained under slow stirring to ensure the hydration of the F127 polymer chains. Subsequently, the 974P polymer was added in small portions until complete solubility was achieved, leading to the formation of the nanogel. Following this, the OE*Pb* was added, and the system was stirred for 30 min. To finalize the organization of the polymer chains, the final solution was refrigerated (5 ºC) overnight, resulting in the nanogel containing OE*Pb*. The preparation of the nanogel containing CUR followed the same methodology, except for the process of incorporating CUR molecules into the F127 copolymeric

micelles, where a direct addition process was employed. In this case, a small amount of F127 was placed in a round-bottom flask containing distilled water at a temperature of 40 ºC with constant stirring. After solubilizing the F127, a quantity of CUR was added to the system and stirred at 40 ºC for 30 min. After cooling the system, the preparation process described for the nanogel containing OE*Pb* was followed to obtain the final material containing both OE*Pb* and CUR (nGPC) as shown in Figure 1A. The empty nanogel (nG) was prepared using the same steps, except the addition of OE*Pb* and CUR.

2.6. Stability Assay of Nanogels

To assess the impact of temperature on the physical and chemical stability of nanogel formulations, accelerated stability tests were conducted in accordance with ANVISA guidelines for Cosmetics and the US Pharmacopeia [31]. A 1 mL aliquot of each formulation was centrifuged at 3000 rpm for 30 minutes at 25 ± 1 °C. The samples were stored under two conditions: ambient temperature (25 ± 3 °C) and controlled refrigeration (5 ± 3 °C), with continuous temperature monitoring throughout the study. Stability was further evaluated by subjecting the formulations to seven alternating cycles of 24 hours at 5 °C followed by 24 h at 25 °C. Physical stability was analyzed based on homogeneity, phase separation, and organoleptic characteristics such as appearance, color, and odor.

2.7. FTIR Analysis

Fourier transform infrared spectroscopy (FTIR) analyses were performed in reflectance mode using a Shimadzu FTIR Tracer-100 spectrophotometer (Kyoto, Japan). The lyophilized samples of nG, nG*P*, and nG*PC* were compressed into pellets with KBr, while pure OE*Pb* was analyzed using the Attenuated Total Reflectance (ATR) mode. For ATR-FTIR measurements, a ZnSe crystal window (PIKE Technologies) was employed. Spectra were acquired within the 400–4000 cm^{-1} range, with a resolution of 8 cm^{-1} and 50 scans per sample. To ensure accurate spectral acquisition, the samples were uniformly distributed over the ATR crystal surface, and the crystal window was thoroughly cleaned with hexane and acetone before subsequent measurements.
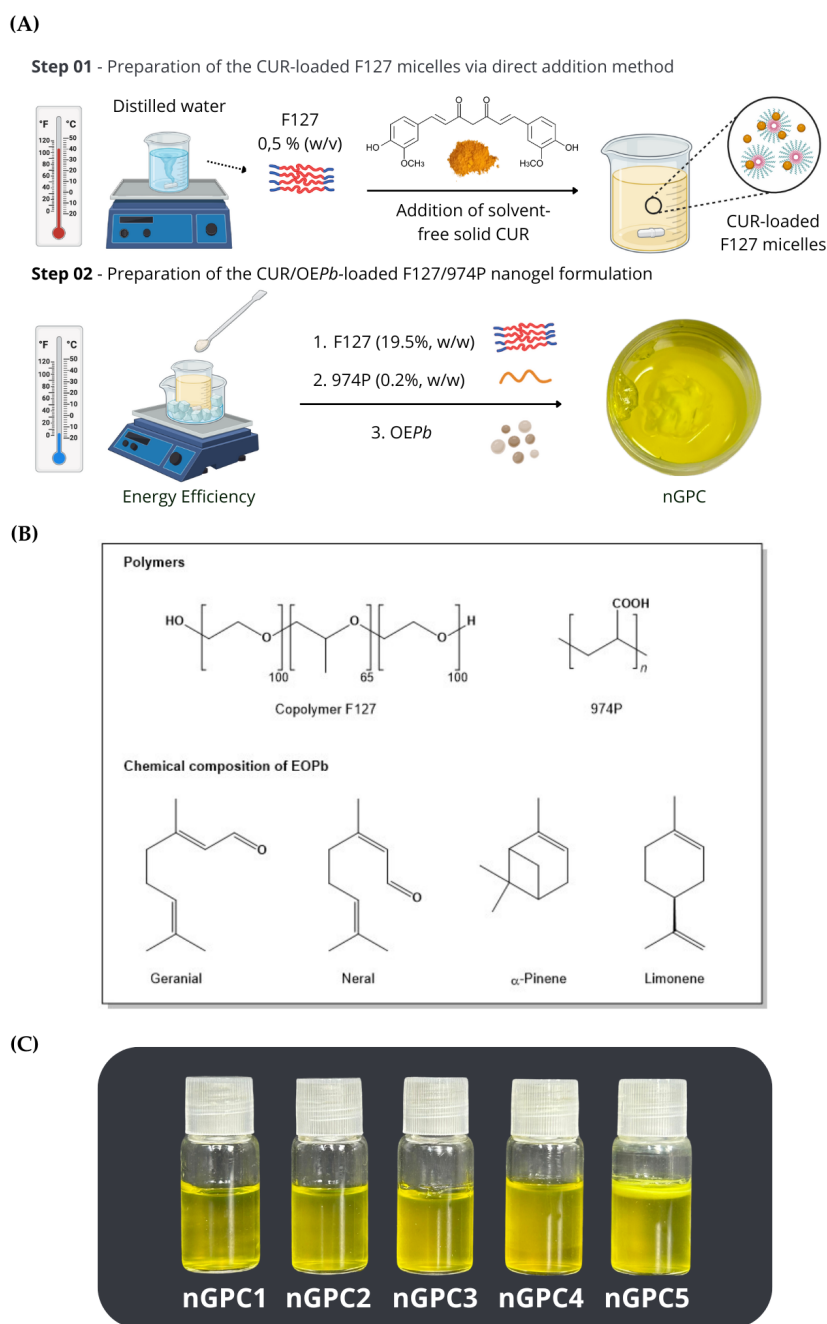
Figure 1. (A) Stages of preparation of nGPC with the addition of CUR to the solution under controlled temperature conditions, ensuring its uniform dispersion within the polymeric matrix. (B) Chemical structure of the polymers used in the preparation of the nanogels and chemical composition of the major chemical constituents of EO*Pb*. (C) Photographs of the nG*P*C1–nG*P*C5 formulations following the accelerated stability test, where the nG*P*C5 nanogel exhibits phase separation.

2.8. Scanning Electron Microscope (SEM)

The morphological analysis of nanogels nG and nGPC was performed using SEM. Initially, the sample was rapidly frozen in liquid nitrogen at -196 °C, followed by a 24 h lyophilization process using a Thermo Micro Modulyo freeze dryer (Thermo Electron Corporation, Pittsburgh, PA, USA). To enhance imaging contrast, a thin metallic coating was applied using a BAL-TEC SCD 050 Sputter Coater (Balzers, Liechtenstein). After lyophilization, the samples were coated with a thin layer of metal using a BAL-TEC SCD 050 Sputter Coater (Balzers, Liechtenstein), and their morphology was analyzed

at magnifications of 100x and 50x using a FEI Quanta 250 microscope (Thermo Fisher Scientific, Karlsruhe, Germany).

2.9. DLS Analysis

Particle size, polydispersity index (PDI) and diffusional thermodynamic parameters of activation measurements were conducted using dynamic light scattering (DLS) with a Litesizer™ 500 instrument (Anton Paar GmbH, Graz, Austria) (BM 10 module). The average hydrodynamic diameters (D_h) of the nanogels nG and nGPC were determined in ultrapure water at temperatures of 25, 32, 37, e 45 °C, using a 40 mW semiconductor laser with a wavelength of 658 nm. D_h measurements were performed in a 3.0 mL quartz cuvette. All measurements were conducted in triplicate (mean ± SD). The diffusion coefficients (D_{if}) were calculated from the D_h values using the Stokes-Einstein equation, assuming the formation of non-interacting spherical particles (Equation (1)) [32].

$$D_{\mathrm{if}} = \frac{k_B T}{6\pi\eta R_h} \tag{1}$$

Where k_B is the Boltzmann constant ($1.3806503 \times 10^{-23}$ J K^{-1}), T is the absolute temperature (K), and η is the viscosity of the medium (Pa s^{-1}). To obtain the values of the diffusional activation energy (E_{ad}), as well as the diffusional entropy ($\Delta S_d^\#$) and enthalpy ($\Delta H_d^\#$), the Arrhenius and Eyring models, adapted for the diffusion process, were employed. The E_{ad} is determined using the following Arrhenius equation (Equation (2)) [33,34]:

$$D_{\mathrm{if}} = A e^{-\frac{E_{\mathrm{ad}}}{RT}} \tag{2}$$

Where D_{if} is the diffusion coefficient, A is the pre-exponential Arrhenius factor, R is the gas constant (8.314 J K^{-1} mol^{-1}), and T is the absolute temperature in K. The plot of $\ln D_{\mathrm{if}} = \ln A - \frac{E_{\mathrm{ad}}}{RT}$ gives E_{ad} by means of the slope. The calculations of $\Delta S_d^\#$ and $\Delta H_d^\#$ are obtained by the adapted Eyring model for diffusion, (Equation (3)):

$$D_{\mathrm{if}} = \frac{RT}{Nh} e^{\frac{\Delta S_d^\#}{R}} e^{-\frac{\Delta H_d^\#}{RT}} \tag{3}$$

Where $N = 6.02 \times 10^{23}$ mol^{-1}, and $h = 6.626 \times 10^{-34}$ J s. The plot of $\ln(D_{\mathrm{if}}T) = \ln\left(\frac{RT}{Nh} e^{\frac{\Delta S_d^\#}{R}} - \frac{\Delta H_d^\#}{RT}\right)$ gives the $\Delta H_d^\#$ using the angular coefficient, and the linear coefficient gives the $\Delta S_d^\#$. The enthalpy of activation ($\Delta H_d^\#$) is obtained from the slope of the plot of $\ln D_{\mathrm{if}}T$, while the entropy of activation ($\Delta S_d^\#$) is obtained from the linear coefficient. Finally, the variation in the diffusive Gibbs free energy ($\Delta G_d^\#$) is calculated using Equation (4) [35,36]:

$$\Delta G_d^\# = \Delta H_d^\# - T\Delta S_d^\# \tag{4}$$

2.10. Rheological Analysis

The rheological properties of the nGPC were evaluated using a controlled-stress rheometer (MARS II, Haake Thermo Fisher Scientific Inc., Germany) equipped with a parallel plate geometry consisting of a steel cone (C35/2° Ti) with a diameter of 35 mm and a fixed gap of 0.105 mm. All measurements were conducted at a controlled temperature of 5, 25, and 32 °C . Before analysis, the samples were equilibrated for 1 minute to ensure thermal and structural stabilization. Flow curves were obtained by applying shear rates in two phases: an upward ramp from 0 to 500 s^{-1} and a downward ramp from 500 to 0 s^{-1}. Each phase lasted 150 seconds, ensuring steady-state conditions were reached before transitioning between ramps. This protocol allowed the assessment of the shear-thinning behavior and any potential hysteresis effects in the nGPC.

2.11. In Vitro Assay Against LLa Promastigotes Cells

LLa (strain PH8) cells were cultured in 199 culture medium supplemented with 10% inactivated fetal bovine serum and antibiotics (100 UI/mL penicillin and 0.1 mg/mL streptomycin). The cultures were incubated at 27 °C with constant subculturing. In 96-well plates, the culture of LLa promastigotes was seeded in RPMI 1640 medium, resulting in a final concentration of 2×10^7 Leishmania/mL after the addition of the compounds. The nGPC nanogel was prepared with 2 mg of OEPb and 0.7 mg of CUR, diluted in RPMI 1640 medium. It was then applied at concentrations ranging from 17.5 µg/mL to 2.19 µg/mL for OE*Pb*, and from 50 µg/mL to 6.25 µg/mL for CUR. For the evaluation of the nanogel containing the combination of OEPb and CUR, the concentrations and dilutions tested were the same as those for the isolated compounds. The plates were then incubated at 27 °C for 24, 48, and 72 h. The viability of the promastigotes was determined using the colorimetric XTT method (2,3-bis(2-methoxy-4-nitro-5-sulfophenyl)-5-[(phenylamino)carbonyl]-2H-tetrazolium hydroxide). A mixture containing 20% XTT and PMS (N-methyl dibenzopyrazine methyl sulfate) and 60% 0.9% saline was added to the plates. The plates were then incubated for 4 hours at 37 °C with 5% CO_2. After this period, absorbance was measured using a spectrophotometer with filters set to 450/620 nm, and the percentage of inhibition was estimated by comparison with untreated cells. Amphotericin B was used as a positive control. The experiments were conducted in triplicate and in the absence of light. The percentage of mortality was calculated based on a logarithmic regression of the control curve made only with Leishmania and culture medium, starting with a concentration of 2×10^7 Leishmania/mL and diluted in a ratio of two down to a concentration of 6.25×10^5 Leishmania/mL.

2.12. Statistical Analysis

The statistical analysis was conducted using a single-criterion method, employing ANOVA followed by Tukey's post-test for pairwise comparisons and Kruskal-Wallis with Dunn's post-hoc test for non-parametric data. Statistical significance was assessed according to predefined criteria. All analyses and graphical representations were carried out with Prism 9 software (GraphPad, San Diego, CA, USA) and Origin Pro software (version 8.5). Statistically significant differences were indicated.

3. Results and Discussion

3.1. Development of Nanogels

Before the preparation of the nanogels, the chemical composition of OE*Pb* was analyzed using GC-MS, revealing a total of nineteen components, which account for 92.66% of the oil's composition. Of these, 64.58% are oxygenated monoterpenes, represented by the isomers geranial (36.06%) and neral (28.52%), while the remaining compounds include *α*-pinene (15.72%) and limonene (8.28%). The chemical structures of the major compounds were confirmed through ^{1}H and ^{13}C NMR [14] and are represented in Figure 1B. According to previous studies, various combinations of F127 and 974P percentages were tested to find the optimal formulation that would allow the thermoresponsive behavior of the nanogel, particularly a rapid sol-gel transition [13,14]. The combinations of 5-10/0.1-0.3% resulted in liquid formulations at 5 and 30 °C, showing no thermoresponsive behavior. In contrast, formulations of 20/0.1-0.3% remained liquid at 5 °C and transitioned to a semi-solid state at 30 °C, with a transition time of approximately 10 min. The 20/0.1 combination produced a low-viscosity formulation, while the 20/0.3 resulted in high-viscosity formulations. The optimal formulation was identified as 20/0.2, which served as the foundation for incorporating OE*Pb* into the nG formulation, characterized by a rapid sol-gel transition.

Furthermore, stability tests showed that adding up to 1% OE*Pb* resulted in stable and transparent formulations, with no phase separation observed after the accelerated stability tests. However, concentrations above this threshold led to formulations with low stability, exhibiting creaminess and phase separation. For this study, the F127/974P/OE*Pb* ratio was fixed at 20/0.2/1% (w/w) and CUR was added at concentrations ranging from 0.01 to 0.05% (w/w), resulting in the formulations, as outlined in Table 1. This was accomplished by testing the maximum amount of CUR that could be

incorporated into the gel matrix containing 1% (w/w) OE*Pb*, followed by an evaluation of the system's accelerated stability. Formulations containing up to 0.03% CUR (nGPC1-nGPC4) remained stable even after being subjected to accelerated stability testing (7 cycles) and shelf-life testing over 180 days Figure 6D. However, when the CUR content exceeded 0.04%, phase separation was observed in nanogel nGPC5 within 48 h of preparation Figure 1C. Therefore, the nGPC4 formulation, which exhibited the highest percentage of the bioactive compounds CUR-OE*Pb*, was selected for further characterization and designated throughout the study as nGPC.

Table 1. Different compositions (% w/w) of CUR and water, were incorporated into the GF2020Pb formulation base to achieve nGPC1 to nGPC4.

	Components % (w/w)					
Code	**Water**	**F127**	**974p**	**EOPb**	**CUR**	**Stability**
nGPC1	78.99	20	0.2	1	0.01	S
nGPC2	78.78	20	0.2	1	0.02	S
nGPC3	78.47	20	0.2	1	0.03	S
nGPC4	78.36	20	0.2	1	0.04	S
nGPC5	78.25	20	0.2	1	0.05	PS

S: Stable; PS: Phase Separation.

3.2. Characterization of Nanogels

3.2.1. FTIR

Figure 2 displays the FTIR spectra of the nanogels nG, nGP, and nGPC. The analysis of the nG spectrum (Figure 2A) reveals a broad and intense absorption band at 3384 cm^{-1}, overlapping with the band at 3564 cm^{-1}. Due to the miscibility of 0.2% 974P in 20% (w/w) F127, part of the 974P-974P and F127-F127 intermolecular interactions is replaced by the formation of F127-974P crosslinked hydrogen bonds. The band observed at 3384 cm^{-1} in the nG spectrum is related to a higher-energy O—H stretch, with a blue shift ($\Delta\nu = 180$ cm^{-1}). However, a relatively large proportion of F127-F127 hydrogen bonds remain present, as indicated by the strong and broad absorption band at 3564 cm^{-1}, which justifies the coexistence of micellar structures of F127 in the nanogel composition. Figure 2B shows the FTIR spectrum of the nG*P* nanogel.

The presence of 1% OE*Pb* in the nG matrix significantly alters the absorption bands associated with the F127/974P blend. The strong, sharp band at 3676 cm^{-1} results from a pronounced red shift ($\Delta\nu = 112$ cm^{-1})) of the band at 3564 cm^{-1}) observed in the nG spectrum. This finding suggests that less energy is required for O—H stretching, likely due to OE*Pb* molecules disrupting some of the F127-974P interactions to accommodate within the nG*P* matrix pores. Although the 3384 cm^{-1} band in nG is now shifted to 3340 cm^{-1} (a 44 cm^{-1} blue shift), likely due to the formation of new intermolecular hydrogen bonds between F127/974P and the neral and geranial isomers, we believe most OE*Pb* molecules are positioned near the hydrophobic PPO chains of F127. This interpretation is supported by the increased energy needed for the asymmetric C—H stretching, as indicated by the blue shift ($\Delta\nu = 19$ cm^{-1}) from 2904 cm^{-1} (nG) to 2885 cm^{-1} in the nG*P* spectrum (Figure 2B), suggesting a significant increase in hydrophobic interactions within the system.

Figures 2C and 2D show the spectra of the nG*P*C material. The intense band related to O—H stretching is split into three signals. The signals at 3550 and 3475 cm^{-1} are attributed to free O—H stretches of CUR molecules and intermolecular hydrogen bonds between F127/974P and CUR molecules, respectively. The signal at 3414 cm^{-1} is attributed to F127/974P intermolecular hydrogen bonds. The presence of the band at 2885 cm^{-1}, assigned to C—H stretching, suggests that the highly hydrophobic CUR molecules preferentially associate with the PPO chains of F127.
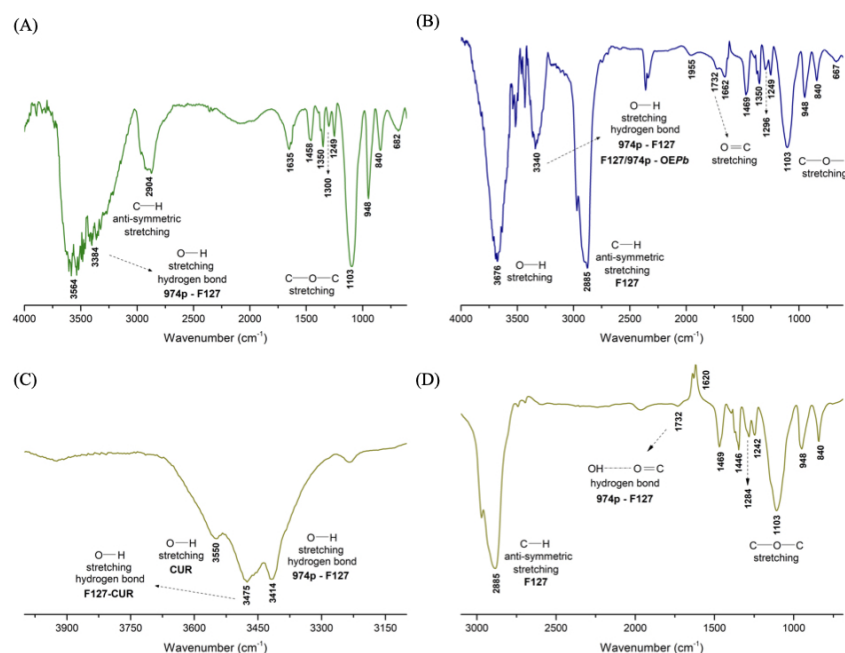
Figure 2. FTIR spectra of the nanogels: (A) nG, (B) nGP (C) nG*P*C in the range of 4000-3100 cm^{-1}, and (D) nG*P*C in the range of 3100-690 cm^{-1}.

3.2.2. SEM

The SEM technique has become an essential tool for exploring the complex structural landscapes of nano and microstructured formulations. Renowned for its exceptional high-resolution imaging capabilities, SEM plays a pivotal role in material characterization at scales highly relevant to pharmaceutical formulations, enabling a detailed understanding of their properties and potential applications. In this study, SEM analysis was employed to investigate the surface and cross-sectional morphology of the freeze-dried nG nanogel. nG micrographs (Figures 3 A and B) reveal that the nG nanogel matrix exhibits a porous architecture, featuring interconnected channel-like structures characteristic of cross-linked F127/974P polymer chains due to intermolecular hydrogen bonding. These morphological characteristics offer valuable insight into the properties of nG, suggesting that its porous network effectively retains the liquid phase containing OE*Pb*/CUR molecules, thereby increasing viscosity through strong hydrogen-bonding interactions with water. In fact, the incorporation of OE*Pb*/CUR into nG induces notable morphological modifications in the nanoformulation. SEM micrographs of nG*P*C reveal a rougher surface texture, suggesting that the pores have been filled, as evidenced by their less defined appearance (Figures 3 C-F). Consistent with FTIR analysis, the strong intermolecular interactions between OE*Pb*/CUR and the PEO polymer chains hinder pore formation during the freeze-drying process.
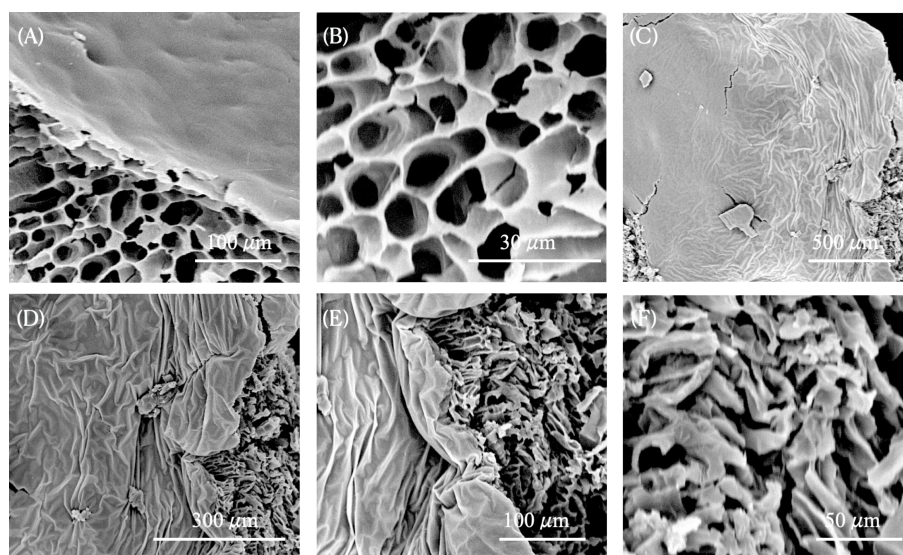
Figure 3. SEM micrographs of nanogels after the freeze-drying process: (A) and (B) nG at magnifications of 1000× and 5000×, respectively; (C), (D), (E), and (F) nG*PC* at magnifications of 200×, 500×, 1000×, and 2000×, respectively.

3.2.3. DLS

The DLS technique is widely used in nanogel characterization due to its ability to accurately measure particle sizes in suspension at the nanoscale [37]. In addition to evaluating the particle size distribution and providing valuable insights into the colloidal stability and intrinsic properties of nanogels, DLS was also fundamental in determining the diffusional thermodynamic parameters of activation. This highlights the crucial role of DLS not only in assessing nanogel stability but also in obtaining key activation parameters that govern their diffusion behavior. This technique is particularly effective in monitoring changes in hydrodynamic diameter (D_h) in response to variations in temperature, pH, and other environmental factors, providing crucial data for developing nanomaterials designed for pharmaceutical and medicinal applications. Analysis of the D_h values for nG reveals a marked reduction in particle size with increasing temperature (Table 2).

DLS measurements were performed on solutions diluted to below 1% (m/v). At these concentrations below the critical micelle concentration (CMC) of F127, the demicellization process is favored, leading to a reduction in the number of smaller particles. This occurs because the total entropy of the system forces smaller particles to aggregate into larger, more polydisperse structures ($D_h = 661$ nm ± 6 and PDI = 0.34). However, since the micellization process of triblock copolymers is highly temperature-dependent, as the temperature of the nG system is increased from 25 to 32 °C, the critical micelle temperature (TMC) compensates for the CMC [38–41]. This results in the formation of smaller particles with reduced polydispersity ($D_h = 124$ nm ± 5 and PDI = 0.24), indicating an increase in the system's total entropy and promoting enhanced particle diffusion, as shown in the analysis of the Diffusivity (D_{if}) as a function of temperature in Figure 4A. This behavior highlights the thermoresponsive nature of the nanogel. At higher temperatures of 32 and 37 °C, the diffusion processes of nG become even more pronounced, leading to a substantial reduction in nanoparticle sizes ($D_h = 17$ nm ± 3 and PDI = 0.25).

Table 2. DLS measurements as a function of temperature for the nG and nG*P*C. Measurements were conducted in quintuplicate, and results are expressed as mean ± SD.

	nG	nGPC
Temperatura (°C)	D_h **(nm) / PDI**	
25	661.00 ± 6.00 / 0.34	288.00 ± 74.00 / 0.29
32	124.00 ± 5.00 / 0.24	296.00 ± 24.00 / 0.44
37	17.00 ± 3.00 / 0.25	237.00 ± 17.00 / 0.42
45	16,93 ± 3.00 / 0.26	333.50 ± 22.00 / 0.45

The decrease in D_h with increasing temperature may be attributed to the dehydration of the PEO groups in the hydrophilic corona and the PPO core at higher temperatures, which leads to a reduction in D_h [41,42]. This process occurs because the rise in thermal energy induces gradual dehydration in non-ionic surfactants, increasing the tendency for separation between the pseudo-phases in the aqueous environment due to shifts in the dynamic equilibrium of micellization. As the temperature increases, the dehydration of both the core and the PEO groups intensifies, causing structural changes in the copolymer. In addition to dehydration, the higher temperature promotes a more efficient entanglement between the PEO and PPO groups, resulting in a significant reduction in the size of the diffusional species in the medium [41,43]. Furthermore, the reduction in D_h could be related to the fact that copolymers with lower molar mass remain as unimers at elevated temperatures. Triblock architecture copolymers, such as F127, exhibit a dynamic equilibrium between unimers and micelles through an insertion-expulsion mechanism, and between micelles of various geometries and sizes via fusion-fragmentation processes [44].

These characteristics, along with the temperature increase, lead to greater friction between the terminal groups due to water molecule extrusion, ultimately promoting an equilibrium shift toward smaller micelles. As temperature rises, the F127 copolymer undergoes structural reorganization driven by dehydration and heightened friction between the copolymer's terminal groups, favoring fragmentation processes and altering the micellization equilibrium [41]. This behavior is primarily attributed to the copolymer's conformation in solution, where the hydrophilic PEO blocks extend beyond the micelle radius, imparting a more fluid nature compared to more hydrophobic copolymers. Additionally, F127 exhibits anomalies related to macromolecular relaxations, primarily due to the conformational changes of the methyl groups in the PPO blocks. These changes are induced by the extrusion of water molecules from the PPO segments as temperature increases. These unique properties of F127 are responsible for its self-diffusion behavior and characteristic micellization equilibria when compared to more hydrophobic copolymers.

The analysis of the D_h values for the nG*P*C material reveals a distinct pattern when compared to the nG material. Unlike nG, the increase in temperature does not significantly reduce the particle size of the nG*P*C material. The observed particle sizes for nGPC, ranging from 237 ± 17 nm to 333 ± 22 nm, are consistent with the stability studies. However, the self-organization dynamics of these materials diverge from those of nG, with the inclusion of OE*Pb*-CUR leading to a reduction in diffusion coefficients (D_{if}) within the system (Figure 4B). The observed decrease in the D_{if} values for nG*P*C can be attributed to the impact of the EO*Pb*-CUR on the self-organization behavior of the nanogel system. The reduction in the diffusion coefficients reflects shifts in the dynamic micellization equilibria, which are influenced by the multicomponent nature of the system. Additionally, copolymers with concentrations ≤ 0.05 g/mL exhibit different aggregation equilibria compared to those at concentrations near or above 0.1 g/mL. These changes in aggregation behavior and thermodynamic properties under varying temperature conditions explain the observed variations in the material's behavior in solution [45].
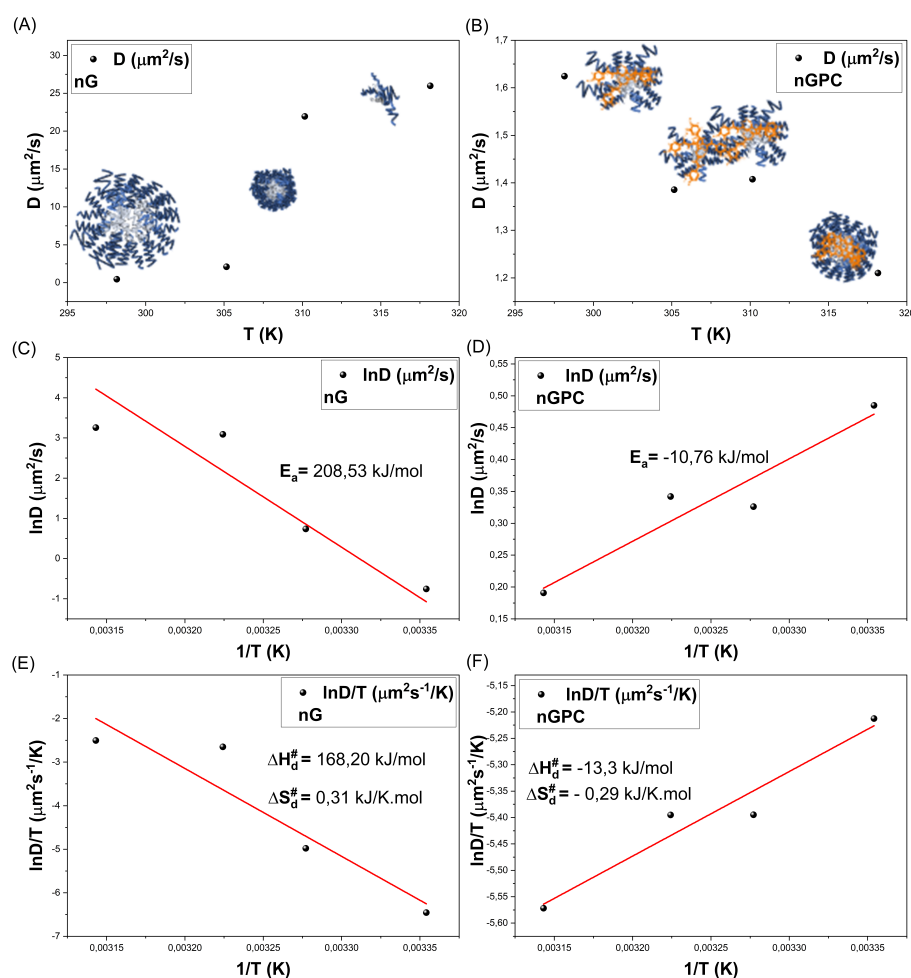
Figure 4. Diffusion Coefficient (D_{if}) as a Function of Temperature (K): Comparative Analysis of (A) nG and (B) nG*P*C.

To gain deeper insights into the effects of temperature, the diffusional activation energy (E_{ad}) and the thermodynamic parameters of diffusion ($\Delta H_d^{\#}$ and $\Delta S_d^{\#}$) were calculated using Arrhenius law (Equation 02) (Figure 4C and 4D) and Eyring's theory (Equation 03) (Figure 4E and 4F), both adapted for diffusion processes [34,45,46]. Activation parameters play a critical role in elucidating the mechanisms underlying diffusion, as they provide insights into the energy required for these processes to occur. For the nG system, the calculated value E_{ad} (greater than zero, as shown in Table 3 confirms the temperature dependence of the diffusion process. Specifically, an E_{ad} of 208.53 kJ/mol indicates that the system utilizes thermal energy to facilitate the diffusion of species in solution. This is accompanied by an enthalpy change ($\Delta H_d^{\#}$) of 168.20 kJ/mol, signifying energy absorption, and an entropy change ($\Delta S_d^{\#}$) of 0.31 kJ/K·mol, reflecting an increase in system disorder.

The temperature rise enhances the hydrophobicity of the copolymer and increases system entropy, leading to the formation of micelles and copolymeric pre-aggregates with smaller hydrodynamic diameters (D_h). This, in turn, increases the excluded volume of the copolymer in solution, which refers to the geometric space occupied by the macromolecular segments. As thermal energy is absorbed, the number of possible configurations available to the system expands, allowing for a broader distribution of species within the nG system and promoting diffusion in the medium. This thermodynamic behavior highlights the adaptability of the system to temperature variations and its potential for temperature-sensitive applications.

The nG*P*C system exhibited a reversal in thermal behavior, with an E_{ad} value of -10.76 kJ/mol, contrasting sharply with the nG system. This shift highlights the impact of incorporating OE*Pb*-CUR, which significantly disrupt the micellization equilibria of the material. At this stage, the thermal energy provided to the system is predominantly utilized in alternative processes, such as structural

reorganization, rather than in mass transport via diffusion. This is evident from the exothermic nature of the process, reflected by a $\Delta H_d^{\#}$ value of -13.30 kJ/mol. The exothermic nature of the diffusion process reveals two key points. First, incorporating OE*Pb*-CUR introduces strong intermolecular interactions between components, resulting in energy release as the system reorganizes itself. This was corroborated by the FTIR analysis, which showed that the more hydrophobic OE*Pb* molecules are preferentially accommodated in the PPO chains of F127. Part of this interpretation is based on the increased energy required for the anti-symmetric stretching of C—H bonds, as indicated by the increased intensity and blue shift ($\Delta \nu = 19$ cm^{-1}) of the band from 2904 cm^{-1} (nG) to 2885 cm^{-1} in the nG*PC* spectrum (Figure 2), indicating a significant increase in the hydrophobic interactions of the system, aligning with the observed enthalpic interaction processes. Second, the decrease in diffusional entropy ($\Delta S_d^{\#} = -0.29$ kJ/K·mol) indicates a reduction in the configurational possibilities of the system. As energy is released, the system becomes more ordered, restricting the range of diffusional configurations.

The synergistic effect of these changes is further validated by *in vitro* applications in cutaneous leishmaniasis. The nG*PC* system demonstrated superior efficacy compared to the control material, underscoring the role of OE*Pb*-CUR in altering the dynamic organization of the nanogel. These incorporations were pivotal in inducing shifts in activation patterns, resulting in an inversion of the diffusional mechanistic behavior. The influence of temperature on the nG and nG*PC* systems is further emphasized by the values of the diffusional Gibbs free energy function ($\Delta G_d^{\#}$) as a function of temperature, presented in Table 3, illustrating the thermodynamic distinctions between the two systems.

The increase in temperature for the nG system leads to a progressive decrease in $\Delta G_d^{\#}$ values, as shown in Figure 5A. This trend indicates that higher temperatures promote diffusion processes, as less energy is required for the micellar systems to diffuse within the solution. This observation aligns with reductions in D_h, $\Delta H_d^{\#}$, and $\Delta S_d^{\#}$, reflecting enhanced micellar dynamics and greater diffusional efficiency at elevated temperatures. In contrast, the nG*PC* system exhibits a thermodynamic inversion with increasing temperature, as previously discussed. This is characterized by negative E_{ad} values and a monotonically increasing trend in $\Delta G_d^{\#}$ (Figure 5B). The system also shows a decrease in $\Delta S_d^{\#}$, indicating molecular reorganization and increased ordering of water molecules to solvate monomeric micelles, micellar pre-aggregates, micelles, and OE*Pb*-CUR as temperature rises. The exothermic $\Delta H_d^{\#}$ values observed with increasing temperature suggest that the transfer of unimers, micellar pre-aggregates, and OE*Pb* from the solution into micelle formation is a thermodynamically favorable process. The hydrophobic PPO segments of the copolymer predominantly drive this phenomenon. This complex thermodynamic mechanism explains the monotonically increasing $\Delta H_d^{\#}$ values: as the system undergoes self-association and structural reorganization, greater energy is required for these processes to progress.

The diffusion mass transfer profiles of both nG and nG*PC* systems reveal complex behaviors. The intrinsic properties of F127, combined with the incorporation of OE*Pb*-CUR, amplify the hydrophobic driving forces within the system. These interactions are responsible for the observed structural changes and thermodynamic inversions, further highlighting the intricate relationship between molecular architecture, temperature, and diffusion dynamics.
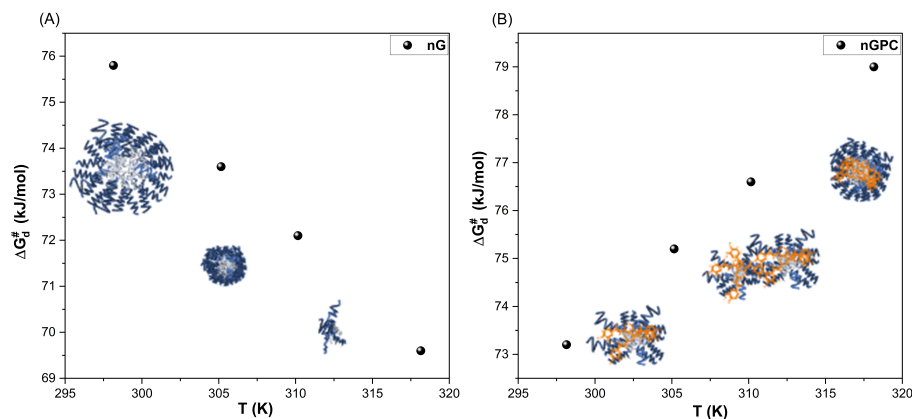
Figure 5. Plot of $\Delta G_d^{\#}$ as a function of temperature for the (A) nG and (B) nGPC nanogel formulations.

Table 3. Thermodynamic parameters of diffusional process for nG and nGPC.

| nG		nGPC	
Parameter	**Value**	**Parameter**	**Value**
E_{ad} (kJ mol^{-1})	208.53	E_{ad} (kJ mol^{-1})	-10.76
$\Delta S^{\ddagger}$ (kJ K^{-1} mol^{-1})	0.31	$\Delta S^{\ddagger}$ (kJ K^{-1} mol^{-1})	-0.29
$\Delta H^{\ddagger}$ (kJ mol^{-1})	168.20	$\Delta H^{\ddagger}$ (kJ mol^{-1})	-13.30
$\Delta G^{\ddagger}$ (kJ mol^{-1}) at different temperatures			
Temperature (K)	**nG**	**Temperature (K)**	**nGPC**
298.15	75.80	298.15	73.20
303.15	73.60	303.15	75.20
305.15	72.10	305.15	76.60
310.15	69.60	310.15	79.00

3.3. Rheological Analysis

The flow curve analysis of the nGPC sample, evaluated up to a shear rate of 1500 s^{-1} at 5 °C, revealed characteristic Newtonian fluid behavior (Figure 6A). The shear stress versus shear rate curve was linear, starting at the origin, and reaching 250 Pa at 1500 s^{-1}. Notably, the forward and backward curves overlapped completely, indicating the absence of hysteresis. This reinforces the rheological stability of the material and rules out thixotropic or rheopectic effects. The constant viscosity, calculated at 0.167 Pa·s, suggests that nGPC maintains uniform rheological properties even at low temperatures such as 5 °C. At 25 °C, the rheological analysis of the nGPC sample demonstrated non-Newtonian behavior, contrasting with the Newtonian characteristics observed at 5°C (Figure 6B). The shear stress versus shear rate curve exhibited shear-thinning behavior, where viscosity decreased with increasing shear rate. This indicates an internal fluid structure that reorganizes under high shear forces, a common characteristic of suspensions or nanogels. The forward curve showed a decrease in shear stress from 200 s^{-1} to 1500 s^{-1}, suggesting viscoelastic or thixotropic responses, while the backward curve was nearly linear, indicating incomplete structural recovery of the fluid.

At 32 °C, the nGPC sample displayed rheological behavior characteristic of non-Newtonian systems, with a pronounced thixotropic pattern (Figure 6C). During the test, the nanogel's viscosity decreased as the shear rate increased, but it did not fully recover after the removal of shear forces. This suggests that the internal structure of the nanogel reorganizes and becomes more fluid under

high-shear conditions. Such behavior is typical of materials where viscosity depends on shear history, as observed in many viscoelastic or thixotropic systems. The forward curve exhibited three peaks followed by drops in viscosity, indicating continuous structural changes within the nanogel as the shear rate increased. However, the structure did not fully restore itself after each peak. This highlights the nanogel's dynamic response to shear, making it easier to apply at high shear rates but with viscosity not returning to its initial state. On the other hand, the backward curve was almost linear but showed a steeper slope than experiments conducted at 25 °C. This indicates that after shear, the sample remained more fluid, with a partially reorganized structure that did not entirely return to its previous condition.

This rheological behavior has significant implications for the topical applications of nG*P*C, particularly at temperatures ranging from 25 to 32 °C, which correspond to typical human skin temperatures. The reduction in viscosity with increasing shear rate facilitates the application of the nanogel, enhancing its spreadability over the skin. The thixotropic behavior, characterized by variations in shear stress, is advantageous for the controlled release of bioactive compounds, enabling a more effective and gradual therapeutic delivery. This profile is especially desirable in topical treatments, as it ensures prolonged and targeted action. Furthermore, the observed rheological stability suggests that the nanogel nG*P*C (Figure 6D maintains its efficacy under physiological conditions, underscoring its strong potential for dermatological applications where stable and controlled performance is critical under varying skin temperatures.
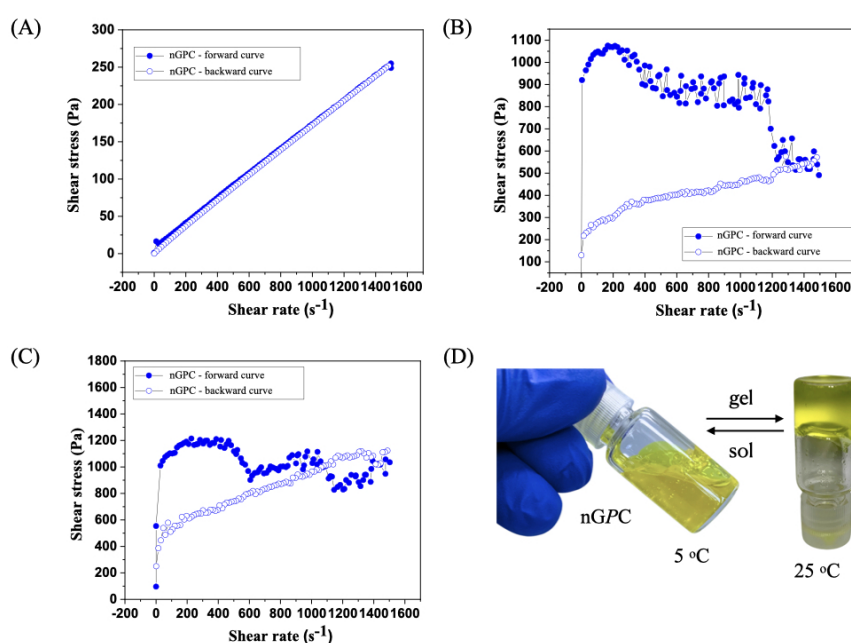
Figure 6. Rheological behavior of the nG*P*C sample at varying temperatures: (A) Newtonian fluid behavior at 5°C with a linear shear stress versus shear rate curve; (B) shear-thinning behavior at 25°C, demonstrating viscosity decrease with increasing shear rate; (C) pronounced thixotropic pattern at 32°C, with viscosity reduction and incomplete structural recovery after shear. The curves demonstrate the nanogel's dynamic response to shear forces, highlighting its suitability for topical applications; (D) real image of the nG*P*C nanogel during the sol-gel transition, showing sol at 5°C and gel at 25°C. The curves demonstrate the nanogel's dynamic response to shear forces, highlighting its suitability for topical applications.

3.4. In Vitro Assay Against LLa Promastigotes

The primary objective of this study was to evaluate whether the therapeutic potential of CUR and OE*Pb*, when incorporated into an F127/974P nanogel matrix, would be preserved in comparison to their free forms in DMSO as a vehicle, as previously described in the literature. Specifically, concentrations of the compounds close to their reported IC_{50} values, when solubilized in DMSO, were selected for this investigation. The study aimed to determine if these concentrations would retain

their biological efficacy when encapsulated in the nanogel matrix, given that the properties of the matrix may influence the bioavailability, release kinetics, and overall therapeutic effectiveness of the active pharmaceutical ingredients (API). It is important to consider that the quantities of excipients used in the preparation of nanogels could negatively influence the cytotoxic potential of API. This is particularly relevant when evaluating the concentration range of the API incorporated into the nanogel formulations, as higher concentrations may lead to increased toxicity, potentially compromising the therapeutic safety profile of the final formulation.

To test this hypothesis, the efficacy of nanogel formulations, including empty nanogels, those containing curcumin, those containing OEPb, and the combination of both compounds, was evaluated. This experimental design allowed for a comprehensive comparison of the effects of each formulation, both in isolation and in combination, thereby providing critical insights into the potential synergistic or additive effects of the CUR-OE*Pb* combination. Furthermore, this setup enabled an assessment of the influence of the nanogel matrix itself on the bioactivity of the compounds by comparing the encapsulated formulations with the free compounds in DMSO. While the encapsulation of the compounds in the nanogel matrix was hypothesized to decrease the immediate bioavailability of CUR and OE*Pb* due to the controlled release mechanism inherent to the nanogel, it was also anticipated that the sustained release properties of the nanogel could offer significant therapeutic advantages. By prolonging the release of the active compounds over time, the nanogel system could potentially enhance the overall therapeutic efficacy, particularly for the treatment of chronic or relapsing diseases such as leishmaniasis. This dual consideration—of potential diminished immediate potency versus prolonged efficacy—forms the basis of the investigation into the effectiveness of these nanogel-based delivery systems.

The effect of the nanogel formulations on *LLa* promastigote cell viability was evaluated at three different time points: 24, 48, and 72 h. Interestingly, the nanogels nG, nGC, and nG*P* showed no anti-promastigote activity at any concentration or time point tested. In contrast, the nanogel nG*P*C demonstrated significant activity, as shown in Figure 7 At the highest concentration tested (17.5 μg/mL of OE*Pb* and 50 μg/mL of CUR), the combination formulation induced over 88% mortality of the promastigotes across all time points (24, 48, and 72 h). This strong effect was observed consistently at each time interval, suggesting a robust and sustained action of the combined compounds. At the lowest concentration tested (2.19 μg/mL of OE*Pb* and 6.25 μg/mL of CUR), the combination formulation still exhibited notable activity, with mortality rates of 24.15%, 21.35%, and 10.40% at 24, 48, and 72 h, respectively. These results demonstrate a dose-dependent effect, with higher concentrations of the combination formulation leading to increased promastigote mortality. The data also suggest a potential synergistic or additive effect between the two compounds, as the combination formulation was more effective than the isolated compounds alone. The findings indicate that the combination of OE*Pb* and CUR, when incorporated into the nanogel matrix, significantly enhances the therapeutic potential against *LLa* promastigote cells.

These findings open up a new avenue of research to better understand the potential synergistic effects of CUR-OE*Pb*. Future studies will aim to elucidate the mechanisms underlying the observed synergism between these API. However, considering that CUR is a potent photosensitizer, complementary studies utilizing PDT are warranted. Such studies will provide insights into the phototherapeutic potential of the nG*P*C system. This approach could pave the way for the discovery of combined therapies, exploring the leishmanicidal action of the nanogel both in the presence and absence of light sources. This line of investigation may significantly expand therapeutic strategies for leishmaniasis, potentially enhancing treatment efficacy through novel, light-activated combinations.
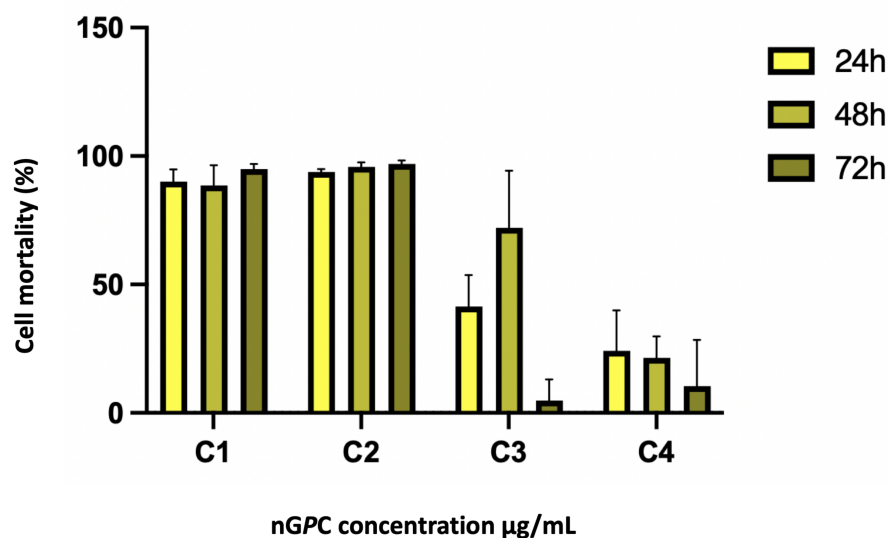
Figure 7. *in vitro* mortality of *LLa* promastigote cells in response to different concentrations of the nG*P*C nanogel formulation across three-time points (24, 48, and 72 h). The concentrations C1-C4 represent the combination of (CUR/OE*Pb*) as follows: C1 = 50:17.5, C2 = 25:8.75, C3 = 12.5:4.38, and C4 = 6.65:2.19 (µg/mL). The data indicate a dose-dependent increase in cell mortality, with the highest concentrations inducing over 88% mortality across all time points.

4. Conclusions

This study demonstrates the potential of the nanogel formulation nG*P*C incorporating CUR and OE*Pb* as a promising therapeutic strategy against *LLa* promastigotes. The physicochemical characterization confirmed the stability, and thermosensitivity of nG*P*C, ensuring its suitability for topical application. Rheological analysis revealed a transition from Newtonian to shear-thinning and thixotropic behavior, facilitating its application in topical treatment. Biological evaluations demonstrated that nG*P*C significantly enhanced anti-promastigote activity compared to free CUR and OE*Pb*, with over 88% mortality at the highest tested concentration and a dose-dependent response at lower concentrations. These findings suggest a synergistic interaction between CUR and OE*Pb*, likely mediated by the nanogel matrix, which improves bioavailability and therapeutic efficacy. The results underscore the potential of nG*P*C in overcoming the limitations of conventional leishmaniasis treatments, particularly by enhancing drug stability, reducing toxicity, and enabling controlled release. Future studies should focus on elucidating the molecular mechanisms underlying the observed synergism, as well as evaluating the impact of PDT to further enhance therapeutic outcomes. The incorporation of light-activated strategies could expand the application of nG*P*C, offering a novel approach for leishmaniasis treatment with improved efficacy and selectivity. Overall, nGPC represents an innovative and effective platform for delivering bioactive compounds against*LLa* promastigotes, reinforcing the relevance of nanotechnology and natural product-based therapies in addressing neglected tropical diseases.

References

1. World Health Organization (WHO). Neglected tropical diseases. *World Health Organization*, 2025. Disponível em: https://www.who.int/news-room/fact-sheets/detail/neglected-tropical-diseases. Acesso em: 2 fev. 2025.

2. Hotez, P. J.; Kamath, A. Neglected tropical diseases in sub-Saharan Africa: review of their prevalence, distribution, and disease burden. *PLoS Neglected Tropical Diseases* **2009**, *3*, e412. DOI: 10.1371/journal.pntd.0000412.

3. Molyneux, D. H.; Savioli, L.; Engels, D. Neglected tropical diseases: progress towards addressing the chronic pandemic. *The Lancet* **2017**, *389*, 312-325. DOI: 10.1016/S0140-6736(16)30171-4.

4. Fitzpatrick, C.; Nwankwo, U.; Lenk, E.; de Vlas, S. J.; Bundy, D. A. P. An Investment Case for Ending Neglected Tropical Diseases. In: Holmes, K. K.; Bertozzi, S.; Bloom, B. R.; Jha, P. (Eds.) *Major Infectious Diseases*; 3rd ed.; The International Bank for Reconstruction and Development / The World Bank: Washington (DC), 2017; Chapter 17.

5. Hotez, P.; Aksoy, S. PLOS Neglected Tropical Diseases: Ten years of progress in neglected tropical disease control and elimination … More or less. *PLoS Neglected Tropical Diseases* **2017**, *11*, e0005355. DOI: 10.1371/journal.pntd.0005355.

6. Ezike, T. C.; Okpala, U. S.; Onoja, U. L.; Nwike, C. P.; Ezeako, E. C.; Okpara, O. J.; Okoroafor, C. C.; Eze, S. C.; Kalu, O. L.; Odoh, E. C.; Nwadike, U. G.; Ogbodo, J. O.; Umeh, B. U.; Ossai, E. C.; Nwanguma, B. C. Advances in drug delivery systems, challenges and future directions. *Heliyon* **2023**, *9*, e17488. DOI: 10.1016/j.heliyon.2023.e17488.

7. Zhang, Y.; Chan, H. F.; Leong, K. W. Advanced materials and processing for drug delivery: The past and the future. *Advanced Drug Delivery Reviews* **2013**, *65*, 104-120. DOI: 10.1016/j.addr.2012.10.003.

8. Cupolillo, E.; Grimaldi, G. Jr.; Momen, H. A general classification of New World Leishmania using numerical zymotaxonomy. *American Journal of Tropical Medicine and Hygiene* **1994**, *50*, 296-311. DOI: 10.4269/ajtmh.1994.50.296.

9. Kato, H.; Uezato, H.; Gomez, E. A.; Terayama, Y.; Calvopiña, M.; Iwata, H.; Hashiguchi, Y. Establishment of a mass screening method of sand fly vectors for Leishmania infection by molecular biological methods. *American Journal of Tropical Medicine and Hygiene* **2007**, *77*, 324-329.

10. Silva, A. C. L.; Oliveira, D. A. P.; Guimarães, C. L.; et al. Leishmania (Leishmania) amazonensis: A review of its biology, clinical manifestations, and treatment. *Revista Brasileira de Parasitologia Veterinária* **2020**, *29*, 560-568. DOI: 10.1590/1678-5150-rbpv-0490.

11. Mann, S.; Frasca, K.; Scherrer, S.; Henao-Martínez, A. F.; Newman, S.; Ramanan, P.; Suarez, J. A. A Review of Leishmaniasis: Current Knowledge and Future Directions. *Current Tropical Medicine Reports* **2021**, *8*, 121–132. DOI: 10.1007/s40475-021-00232-7.

12. da Costa, C. S.; Marques, E. M.; do Nascimento, J. R.; Lima, V. A. S.; Santos-Oliveira, R.; Figueredo, A. S.; de Jesus, C. M.; de Souza Nunes, G. C.; Brandão, C. M.; de Jesus, E. T.; Sa, M. C.; Tanaka, A. A.; Braga, G.; Santos, A. C. F.; de Lima, R. B.; Silva, L. A.; Alencar, L. M. R.; da Rocha, C. Q.; Gonçalves, R. S. Design of Liquid Formulation Based on F127-Loaded Natural Dimeric Flavonoids as a New Perspective Treatment for Leishmaniasis. *Pharmaceutics* **2024**, *16*, 252. DOI: 10.3390/pharmaceutics16020252.

13. Marques, E. M.; Rocha, R. L.; Brandão, C. M.; Xavier, J. K. A. M.; Camara, M. B. P.; Mendonça, C. J. S.; de Lima, R. B.; Souza, M. P.; Costa, E. V.; Gonçalves, R. S. Development of an Eco-Friendly Nanogel Incorporating

Pectis brevipedunculata Essential Oil as a Larvicidal Agent Against *Aedes aegypti*. *Pharmaceutics* **2024**, *16*, 1337. DOI: 10.3390/pharmaceutics16101337.

14. Marques, E. M.; Santos Andrade, L. G.; Rebelo Alencar, L. M.; Dias Rates, E. R.; Ribeiro, R. M.; Carvalho, R. C.; de Souza Nunes, G. C.; Sara Lopes Lera-Nonose, D. S.; Gonçalves, M. J. S.; Lonardoni, M. V. C.; Souza, M. P.; Costa, E. V.; Gonçalves, R. S. Nanotechnological formulation incorporating Pectis brevipedunculata (Asteraceae) essential oil: an ecofriendly approach for leishmanicidal and anti-inflammatory therapy. *Polymers* **2025**, *17*, 379. DOI: 10.3390/polym17030379.

15. Carvalho, C. E.; Sobrinho-Junior, E. P.; Brito, L. M.; Nicolau, L. A.; Carvalho, T. P.; Moura, A. K.; Rodrigues, K. A.; Carneiro, S. M.; Arcanjo, D. D.; Citó, A. M.; Carvalho, F. A. Anti-Leishmania activity of essential oil of Myracrodruon urundeuva (Engl.) Fr. All.: composition, cytotoxicity and possible mechanisms of action. *Experimental Parasitology* **2017**, *175*, 59–67. DOI: 10.1016/j.exppara.2017.02.012.

16. Ferreira, O. O.; Cruz, J. N.; de Moraes, Â. A. B.; de Jesus Pereira Franco, C.; Lima, R. R.; Anjos, T. O. D.; Siqueira, G. M.; Nascimento, L. D. D.; Cascaes, M. M.; de Oliveira, M. S.; Andrade, E. H. A. Essential oil of the plants growing in the Brazilian Amazon: chemical composition, antioxidants, and biological applications. *Molecules* **2022**, *27*, 4373. DOI: 10.3390/molecules27144373.

17. de Lara da Silva, C. E.; Oyama, J.; Ferreira, F. B. P.; de Paula Lalucci-Silva, M. P.; Lordani, T. V. A.; de Lara da Silva, R. C.; de Souza Terron Monich, M.; Teixeira, J. J. V.; Lonardoni, M. V. C. Effect of essential oils on *Leishmania amazonensis*: a systematic review. *Parasitology* **2020**, *147*, 1392–1407. DOI: 10.1017/S0031182020001304

18. Alves, A. B.; da Silva Bortoleti, B. T.; Tomiotto-Pellissier, F.; Ganaza, A. F. M.; Gonçalves, M. D.; Carloto, A. C. M.; Rodrigues, A. C. J.; Silva, T. F.; Nakazato, G.; Kobayashi, R. K. T.; Lazarin-Bidóia, D.; Miranda-Sapla, M. M.; Costa, I. N.; Pavanelli, W. R.; Conchon-Costa, I. Synergistic Antileishmanial Effect of Oregano Essential Oil and Silver Nanoparticles: Mechanisms of Action on *Leishmania amazonensis*. *Pathogens* **2023**, *12*, 660. DOI: 10.3390/pathogens12050660.

19. Alanazi, A. D.; Alghabban, A. J. Antileishmanial and synergic effects of *Rhanterium epapposum* essential oil and its main compounds alone and combined with glucantime against *Leishmania major* infection. *International Journal for Parasitology: Drugs and Drug Resistance* **2024**, *26*, 100571. DOI: 10.1016/j.ijpddr.2024.100571.

20. Monzote, L.; Geroldinger, G.; Tonner, M.; Scull, R.; De Sarkar, S.; Bergmann, S.; Bacher, M.; Staniek, K.; Chatterjee, M.; Rosenau, T.; Gille, L. Interaction of ascaridole, carvacrol, and caryophyllene oxide from essential oil of *Chenopodium ambrosioides* L. with mitochondria in *Leishmania* and other eukaryotes. *Phytotherapy Research* **2018**, *32*, 1729–1740. DOI: 10.1002/ptr.6097.

21. Essid, R., Damergi, B., Fares, N., Jallouli, S., Limam, F., Tabbene, O. Synergistic combination of *Cinnamomum verum* and *Syzygium aromaticum* treatment for cutaneous leishmaniasis and investigation of their molecular mechanism of action. *International Journal of Environmental Health Research* **2024**, *34*, 2687-2701. DOI: 10.1080/09603123.2023.2267470.

22. Santana, R. C., Rosa, A. D. S., Mateus, M. H. D. S., Soares, D. C., Atella, G., Guimarães, A. C., Siani, A. C., Ramos, M. F. S., Saraiva, E. M., Pinto-da-Silva, L. H. In vitro leishmanicidal activity of monoterpenes present in two species of *Protium* (Burseraceae) on *Leishmania amazonensis*. *Journal of Ethnopharmacology*, **2020**, *259*, 112981. DOI: 10.1016/j.jep.2020.112981.

23. Pereira, S. L.; Marques, A. M.; Sudo, R. T.; Kaplan, M. A.; Zapata-Sudo, G. Vasodilator Activity of the Essential Oil from Aerial Parts of *Pectis brevipedunculata* and Its Main Constituent Citral in Rat Aorta. *Molecules* **2013**, *18* (3), 3072–3085. DOI: 10.3390/molecules18033072.

24. Santos, S. R.; Melo, M. A.; Cardoso, A. V.; Santos, R. L.; de Sousa, D. P.; Cavalcanti, S. C. Structure-Activity Relationships of Larvicidal Monoterpenes and Derivatives against *Aedes aegypti* Linn. *Chemosphere* **2011**, *84* (1), 150–153. DOI: 0.1016/j.chemosphere.2011.02.018

25. Limane, B. B.; Ezzine, O.; Dhahri, S.; Ben Jamaa, M. L. Essential Oils from Two Eucalyptus from Tunisia and Their Insecticidal Action on *Orgyia trigotephras* (Lepidoptera, Lymantriidae). *Biol. Res.* **2014**, *47* (1), 29. DOI: 10.1186/0717-6287-47-29.

26. Varzandeh, M.; Mohammadinejad, R.; Esmaeilzadeh-Salestani, K.; Dehshahri, A.; Zarrabi, A.; Aghaei-Afshar, A. Photodynamic therapy for leishmaniasis: Recent advances and future trends. *Photodiagnosis and photodynamic therapy* **2021**, *36*, 102609. DOI: 10.1016/j.pdpdt.2021.102609.

27. Dourado, D.; Silva Medeiros, T.; do Nascimento Alencar, É.; Matos Sales, E.; Formiga, F. R. Curcumin-loaded nanostructured systems for treatment of leishmaniasis: a review. *Beilstein journal of nanotechnology* **2024**, *15*, 37–50. DOI: 10.3762/bjnano.15.4.

28. Albalawi, A. E.; Alanazi, A. D.; Sharifi, I.; Ezzatkhah, F. A Systematic Review of Curcumin and its Derivatives as Valuable Sources of Antileishmanial Agents. *Acta parasitologica* **2021**, *66* (3), 797–811. DOI: 10.1007/s11686-021-00351-1.

29. Haddad, M.; Sauvain, M.; Deharo, E. Curcuma as a parasiticidal agent: a review. *Planta medica* **2011**, *77* (6), 672–678. DOI: 10.1055/s-0030-1250549.

30. Khan, M.; Nadhman, A.; Sehgal, S. A.; Siraj, S.; Yasinzai, M. M. Formulation and Characterization of a Self-Emulsifying Drug Delivery System (SEDDS) of Curcumin for the Topical Application in Cutaneous and Mucocutaneous Leishmaniasis. *Current topics in medicinal chemistry* **2018**, *18* (18), 1603–1609. DOI: 10.2174/1568026618666181025104818.

31. United States Pharmacopeia and National Formulary (USP 41-NF 36); United States Pharmacopeial Convention: **2016**.

32. Alexander, S.; Cosgrove, T.; Prescott, S. W.; Castle, T. C. Flurbiprofen Encapsulation Using Pluronic Triblock Copolymers. *Langmuir* **2011**, *27*, 8054–8060. DOI: 10.1021/la201124c.

33. Haillant, O.; Dumbleton, D.; Zielnik, A. An Arrhenius Approach to Estimating Organic Photovoltaic Module Weathering Acceleration Factors. *Solar Energy Materials & Solar Cells* **2011**, *95*, 1889–1895. DOI: 10.1016/j.solmat.2011.02.013.

34. Griffiths, P. C.; Stilbs, P.; Yu, G. E.; Booth, C. Role of Molecular Architecture in Polymer Diffusion: A PGSE-NMR Study of Linear and Cyclic Poly(ethylene Oxide). *Journal of Physical Chemistry* **1995**, *99*, 16752–16756. DOI: 10.1021/j100045a041.

35. De, M.; Bhattacharya, S. C.; Moulik, S. P.; Panda, A. K. Interfacial Composition, Structural and Thermodynamic Parameters of Water/(Surfactant+n-Butanol)/n-Heptane Water-in-Oil Microemulsion Formation in Relation to the Surfactant Chain Length. *Journal of Surfactants and Detergents* **2010**, *13*, 475–484. DOI: 10.1007/s11743-010-1186-7.

36. Hwang, D.; Ramsey, J. D.; Kabanov, A. V. Polymeric micelles for the delivery of poorly soluble drugs: From nanoformulation to clinical approval. *Advanced Drug Delivery Reviews* 2020, *156*, 80–118.

37. Chakraborty, M.; Panda, A. K. Spectral Behaviour of Eosin Y in Different Solvents and Aqueous Surfactant Media. *Spectrochimica Acta Part A: Molecular and Biomolecular Spectroscopy* **2011**, *81*, 458–465. DOI: 10.1016/j.saa.2011.06.038.

38. Alexandridis, P.; Hatton, T. A. Poly(ethylene Oxide)-poly(propylene Oxide)-poly(ethylene Oxide) Block Copolymer Surfactants in Aqueous Solutions and at Interfaces: Thermodynamics, Structure, Dynamics, and Modeling. *Colloids and Surfaces A: Physicochemical and Engineering Aspects* **1995**, *96*, 1–46. DOI: 10.1016/0927-7757(94)03028-X.

39. Wanka, G.; Hoffmann, H.; Ulbricht, W. Phase Diagrams and Aggregation Behavior of Poly(oxyethylene)-Poly(oxypropylene)-Poly(oxyethylene) Triblock Copolymers in Aqueous Solutions. *Macromolecules* **1994**, *27*, 4145–4159. DOI: 10.1021/ma00093a016.

40. Alexander, S.; Cosgrove, T.; Castle, T. C.; Grillo, I.; Prescott, S. W. Effect of Temperature, Cosolvent, and Added Drug on Pluronic–Flurbiprofen Micellization. *Journal of Physical Chemistry B* **2012**, *116*, 11545–11551. DOI: 10.1021/jp303185m.

41. Brown, W.; Schillin, K. Triblock Copolymers in Aqueous Solution Studied by Static and Dynamic Light Scattering and Oscillatory Shear Measurements: Influence of Relative Block Sizes. *American Chemical Society* **1992**, *6044*, 6038–6044.

42. Sharma, P. K.; Bhatia, S. R. Effect of Anti-Inflammatories on Pluronic® F127: Micellar Assembly, Gelation and Partitioning. *International Journal of Pharmaceutics* **2004**, *278*, 361–377. DOI: 10.1016/j.ijpharm.2004.03.029.

43. Nilsson, M.; Håkansson, B.; Söderman, O.; Topgaard, D. Influence of Polydispersity on the Micellization of Triblock Copolymers Investigated by Pulsed Field Gradient Nuclear Magnetic Resonance. *Macromolecules* **2007**, *40*, 8250–8258. DOI: 10.1021/ma071302p.

44. Landazuri, G.; Fernandez, V. V. A.; Soltero, J. F. A.; Rharbi, Y. Kinetics of the Sphere-to-Rod like Micelle Transition in a Pluronic Triblock Copolymer. *Journal of Physical Chemistry B* **2012**, *116*, 11720–11727. DOI: 10.1021/jp3009089.

45. Brown, W.; Stilbs, P. On the Solution Conformation of Poly(ethylene Oxide): An FT-Pulsed Field Gradient NMR Self-Diffusion Study. *Polymer* **1982**, *23*, 1780–1784. DOI: 10.0032/3861/82/121780.

46. Espenson, J. H. *Chemical Kinetics and Reaction Mechanisms*. Second Edition. McGraw-Hill Series in Advanced Chemistry, **1995**.